# The ammonia absorption spectrum between 4700 and 5650 cm − 1

P. Cacciani, P. Čermák, J. Vander Auwera, A. Campargue

* Corresponding author: E-mail: alain.campargue@univ-grenoble-alpes.fr

# The ammonia absorption spectrum between 4700 and 5650 $cm^{-1}$

P. Cacciani

*Laboratoire de Physique des Lasers, Atomes et Molécules, CNRS, UMR 8523 Université Lille 1, 59655 Villeneuve d'Ascq Cedex, France*

P. Čermák

*Department of Experimental Physics, Faculty of Mathematics, Physics and Informatics, Comenius University, Mlynská dolina, 842 48 Bratislava, Slovakia*

J. Vander Auwera

*Spectroscopy, Quantum Chemistry and Atmospheric Remote Sensing (SQUARES), C.P. 160/09, Université Libre de Bruxelles, 50 avenue F.D. Roosevelt, B-1050 Brussels, Belgium*

A. Campargue*

*Univ. Grenoble Alpes, CNRS, LIPhy, 38000 Grenoble, France*

**Abstract**

Room temperature absorption spectra of ammonia were recorded by high-resolution Fourier transform spectroscopy in the 4700-5600 $cm^{-1}$ range at four pressures (13, 46, 140, and 304 Pa). Additionally, we use an existing Kitt Peak spectrum to extend the analysis up to 5650 $cm^{-1}$. In total, 9110 absorption lines with intensity ranging from $1 \times 10^{-25}$ to $1.6 \times 10^{-20}$ cm/molecule were retrieved, for the two principal isotopologues. Another Kitt Peak spectrum was used to identify 505 $^{15}NH_3$ transitions within the experimental line list. The rovibrational assignments of the $^{14}NH_3$ lines relied on the position and intensity agreement with the C2018 theoretical line list (Coles *et al.* JQSRT 2018;219 199–212) and were validated by the systematic use of Lower State Combination Difference (LSCD) relations. In the process, a number of intensity transfer between nearby transitions were identified. Finally, 6562 transitions were assigned to 61 vibrational bands of the main isotopologue, $^{14}NH_3$, representing 98.85% of the C2018 integrated absorption at room temperature in the region. The upper state empirical energy of a total of 2215 rovibrational levels of $^{14}NH_3$ were derived. Most of them are newly reported. The comparison with the current HITRAN2020 list is discussed. A recommended line list for ammonia in natural isotopic abundance is provided for the studied region.

## 1. Introduction

Ammonia is an essential component in various astrophysical and terrestrial objects, including the Earth's atmosphere. Therefore, understanding its infrared absorption spectra is a prerequisite for accurate monitoring of these environments [1, 2]. This task is made difficult by numerous interactions between its six vibrational modes and the internal inversion motion.

The current work is part of the analysis of the ammonia high resolution spectrum recorded by Fourier Transform Spectroscopy (FTS) in the 3900-5600 $cm^{-1}$ range. The low energy part of the range, from 3900 to 4700 $cm^{-1}$, was covered in our previous contribution [3], while the remainder of the data set, up to 5600 $cm^{-1}$, is analyzed in the

current work. The present FTS data are complemented with an existing Kitt Peak FTS spectrum in the weak absorbing 5600-5650 $cm^{-1}$ interval, in order to fill the gap up to our previous analysis of the 5650-6350 $cm^{-1}$ range [4].

The HITRAN line list [5] in the considered range is based on the study of a FTS spectrum recorded at Kitt Peak with a 0.011 $cm^{-1}$ spectral resolution [6]. The spectrum is dominated by the $\nu_1 + \nu_4$ and $\nu_3 + \nu_4$ bands centered at 4956 $cm^{-1}$ and 5050 $cm^{-1}$, respectively. The upgrade of the HITRAN database from 2016 [7] to 2020 [5] has increased the number of $^{14}NH_3$ transitions from 1875 to 2493 while the $^{15}NH_3$ dataset in the region has remained unchanged. The overview of HITRAN2020 list is presented in the upper panel of Fig. 1. About 620 new transitions of $^{14}NH_3$ included in HITRAN2020 were not observed but transferred from the hybrid CoYuTe list created by adjusting the line positions predicted from the C2018 potential energy surface [8] according to empirical energy levels determined using the MARVEL algorithm [9]. For the HITRAN2020 edition [5], it was decided to add to the HITRAN2016 dataset [7] only the CoYuTe transitions for which both the lower and upper levels have empirical energies and their calculated line intensities are larger than $1\times10^{-25}$ cm/molecule. In our region, the added transitions include several hot band transitions for which the upper levels were determined from ground state transitions, thus at higher energy [10]. Their intensities are generally less than $3 \times 10^{-24}$ cm/molecule which was the intensity cut-off of the HITRAN2016 list. Among the $^{14}NH_3$ transitions, 1255 are given with full assignment of the lower and upper states, whereas no or incomplete assignment is given for 1201 transitions. Experimental intensities have been kept for the transitions transferred from HITRAN2016, whereas C2018 calculated intensity values [11] are given for the added transitions.

Regarding the previous experimental studies in our region, in addition to Ref. [6], it is worth mentioning the recent work of Beale *et al.* [12]. These authors reported an analysis of ammonia FTS spectra recorded at different temperatures from 295 to 973 K with a 0.01 $cm^{-1}$ spectral resolution. Due to its lower accuracy, this study was used neither for the HITRAN2020 update nor for the derivation of new MARVEL energy levels [11]. Nevertheless, it is a very useful source for the application of Lower State Combination Differences (LSCD) relations used for validation of our quantum assignments [4].

As the experimental setup, conditions of the recordings, fitting process and construction of the line list were detailed in Ref. [3], they are briefly recalled in the two next sections. Section 4 describes some aspects of the assignment process before discussing the results in particular the occurrence of intensity transfers between resonant lines.

## 2. Experimental details

The experimental conditions of the measurements are summarized in Table 1. Four room temperature FTS absorption spectra of ammonia were recorded at ULB with a Bruker IFS 120 (upgraded to 125) spectrometer in the 3900-5600 $cm^{-1}$ range (Fig. 2).

To supplement these data, we used a couple of FTS spectra from the National Solar Observatory historical archive recorded in early nineties at Kitt Peak observatory. To fill the 5600-5650 $cm^{-1}$ interval of weak ammonia absorption we used a long-path recording (KP1, Ref. 900308R0.019), and to identify the $^{15}NH_3$ transitions, an ammonia spectrum enriched in $^{15}NH_3$ (KP2, 930826R0.016) was treated.

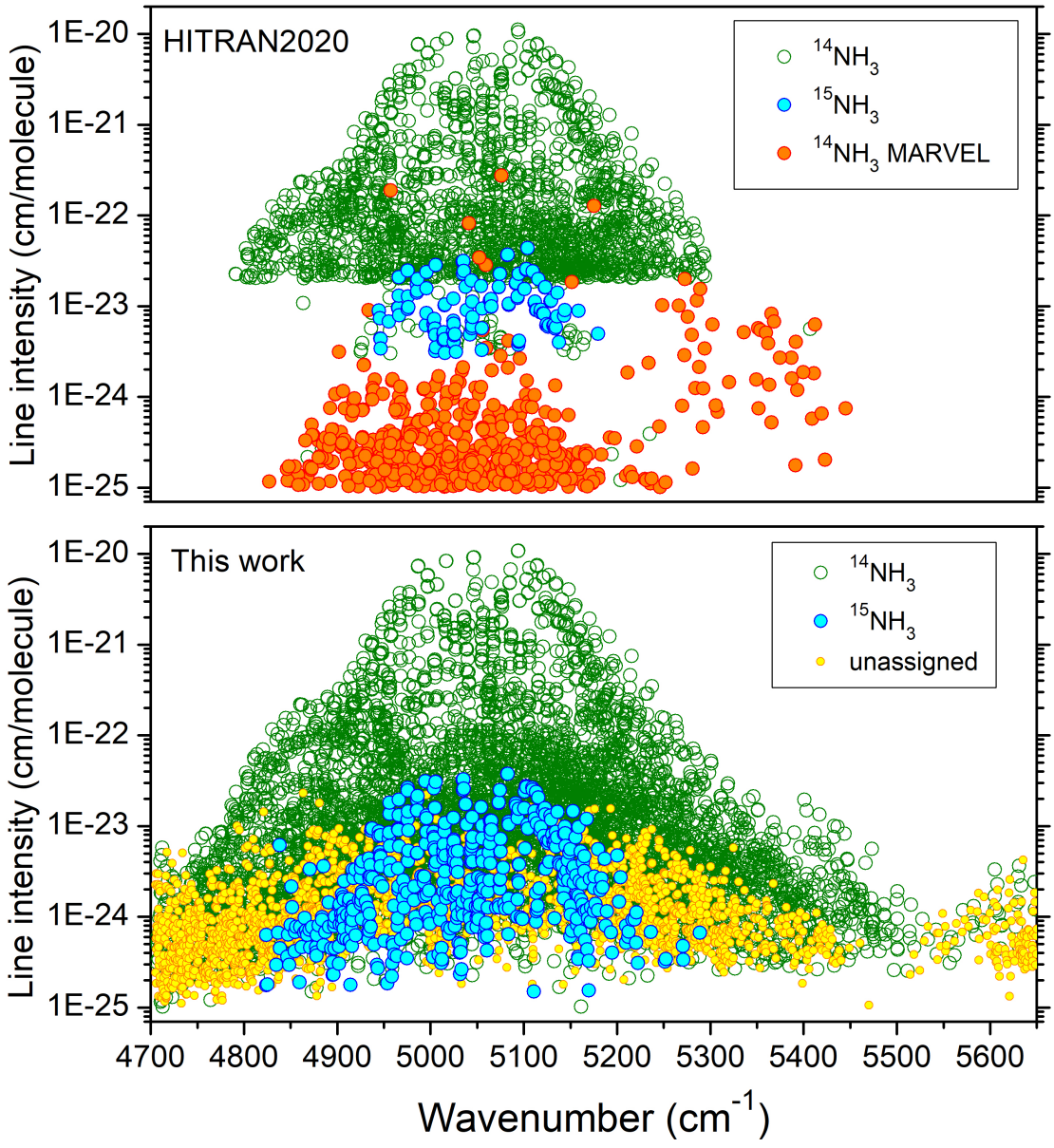


Figure 1: *Upper panel*: Overview of the HITRAN2020 transitions of $^{14}NH_3$ (green and orange) and $^{15}NH_3$ (cyan) in the studied region. $^{14}NH_3$ transitions were added using MARVEL algorithm (orange). *Lower panel*: Ammonia transitions measured in the present work: $^{14}NH_3$ and $^{15}NH_3$ (green and cyan circles, respectively), and unassigned (yellow circles).

Table 1: Experimental parameters of the four FTS spectra used in this work.

| Spectrum | $p$ (Torr) | $p$ (Pa) | $c_{^{15}N}$ (%) | $L$ (m) | $R$ ($cm^{-1}$) |
|---|---|---|---|---|---|
| TW1 | 0.109 (6) | 13.2 (1.5) | 0.78 | 13.86 (4) | 0.003 |
| TW2 | 0.348 (8) | 46.0 (1.1) | 0.68 | | |
| TW3 | 1.053 (33) | 140.4 (4.4) | 0.62 | | |
| TW4 | 2.28 (8) | 304.0 (11.0) | 0.54 | | |
| KP1 (Ref. 900308R019) | 0.52 | 69.3 | | 193 | 0.01 |
| KP2 ($^{15}NH_3$ - Ref. 930826R016) | 2.0 | 167. | 99.64 | 16 | 0.01 |

Notes: For the four spectra studied in this work (TW1-TW4), $p$ is the average pressure (the numbers between parentheses are the uncertainties of measurement, provided in the units of the last digit quoted, $L$ is the interaction pathlength and $R$ is the spectral resolution used for the recording. $c_{^{15}N}$ is the estimated value of the $^{15}NH_3$ relative abundance (the natural value is 0.37%).

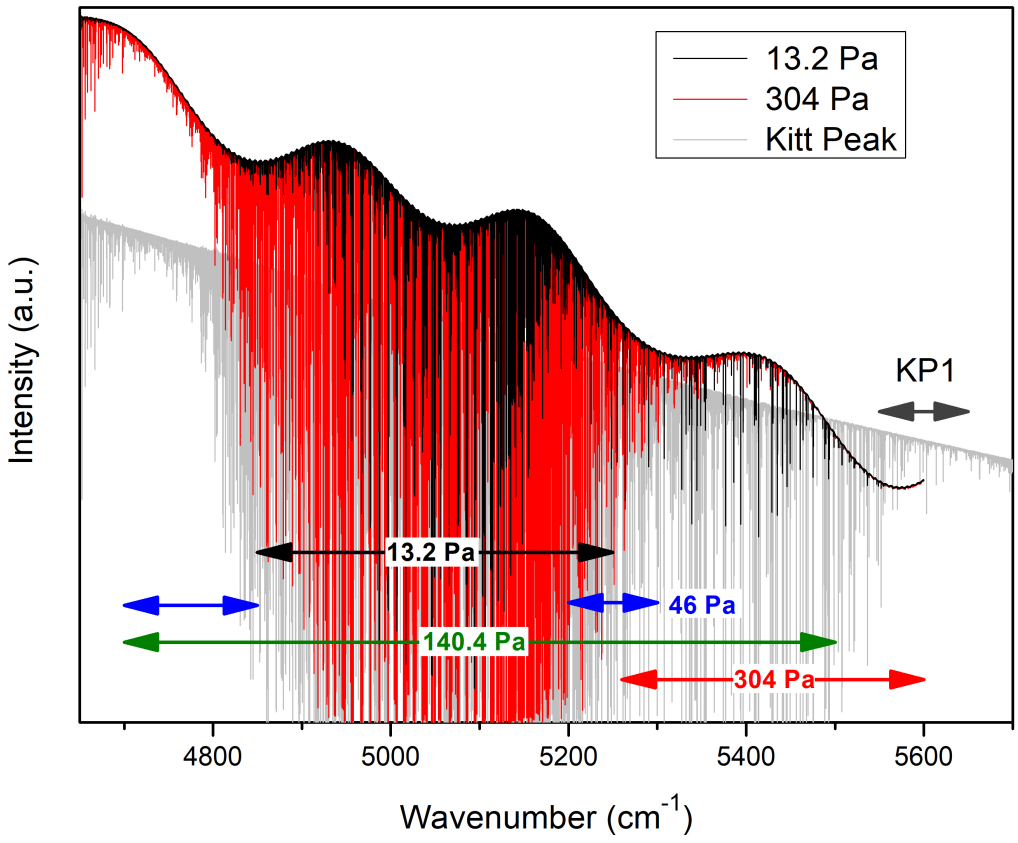


Figure 2: Overview of the Fourier transform absorption spectra of ammonia recorded in the present work with the resolution of 0.003 $cm^{-1}$. The arrows mark the spectral intervals of the spectra used in the analysis. In the 5600-5650 $cm^{-1}$ interval, the Kitt Peak spectrum (KP1) with Ref. 900308R0.019 was used.

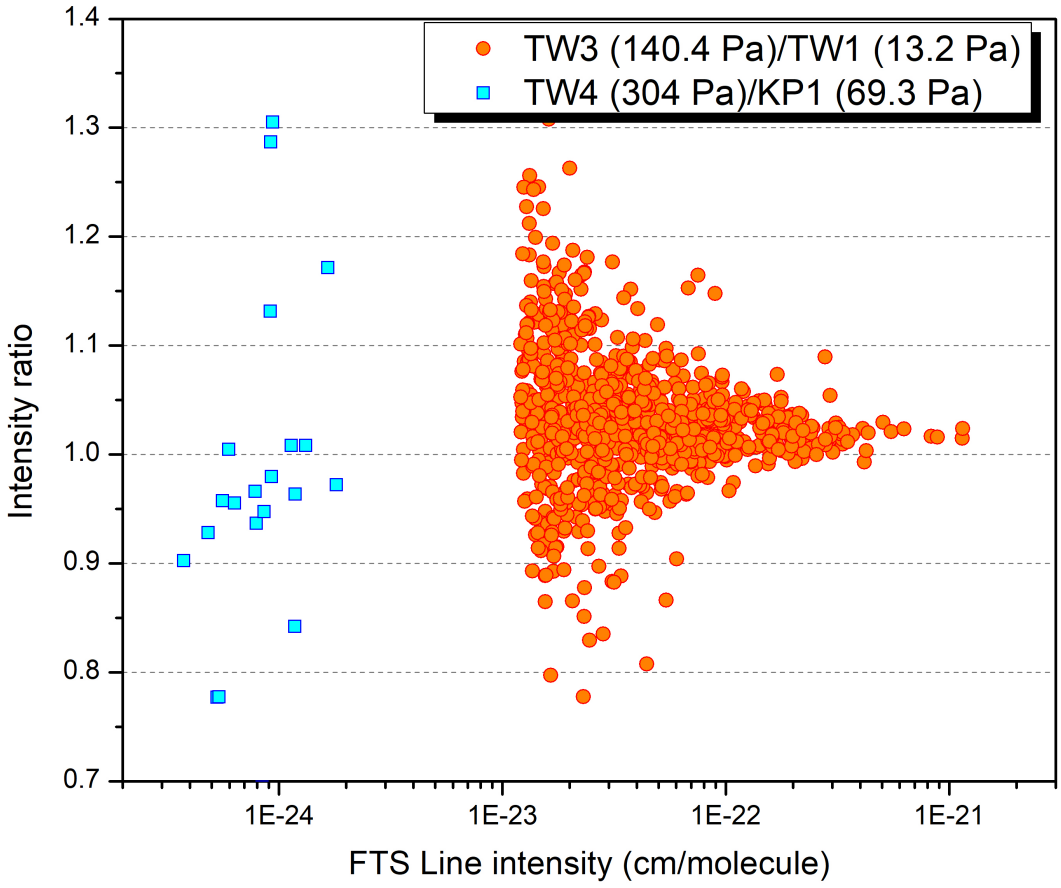


Figure 3: Ratios of the intensities derived from the 140.4 Pa spectrum to those of the 13.2 Pa spectrum (orange dots) for isolated transitions in the $1.2 \times 10^{-23}$ - $1.2 \times 10^{-21}$ cm/molecule range. $^{15}NH_3$ transitions were removed from the comparison. Intensity ratios between the KP1 Kitt Peak spectrum and the 304 Pa spectrum are plotted for a few weak lines below 5600 $cm^{-1}$ (cyan dots). They are used for the intensity calibration of the 5600-5650 $cm^{-1}$ interval.

## 3. Line list construction

Line positions and line intensities were retrieved using a multi-line fit of the spectra. The fit was performed assuming a simple Voigt function as line profile, thus, including in an effective way the Instrument Line Shape (ILS). The Lorentzian and Gaussian components of the Voigt profile were assumed to be identical for all the lines and adjusted in the fit. The fitted value of the Gaussian width was found slightly above the calculated value of the $^{14}NH_3$ Doppler broadening (FWHM 0.015 $cm^{-1}$), confirming a small contribution of ILS. Constraining the line widths helped to disentangle blended lines.

In Ref. [3], it was demonstrated that our data treatment neglecting the ILS leads to underestimated line intensities in case of strong absorbance, and the correction of this bias was presented. The same process was applied in the current range. As a test of the correction and consistency of the intensity values in this new range, Fig. 3 plots the

ratio of intensities retrieved from different sources. The intensities from the 140.4 Pa spectrum are compared to those retrieved from of the 13.2 Pa spectrum. For the KP1 data in the 5550-5600 $cm^{-1}$ interval, the intensity ratio between the 304 Pa and the KP1 spectra is presented for a few lines. Isolated lines were preferred for the comparison (minimum position separation of 0.03 $cm^{-1}$). The oscillator strength spans over two orders of magnitude between $1.2 \times 10^{-23}$ and $1.2 \times 10^{-21}$ cm/molecule (in order to correspond to absorbances not too small at 13.2 Pa spectrum and not too large at 140.4 Pa). On average, a small overestimation of 1.5% is noted between $1.2 \times 10^{-22}$ and $1.2 \times 10^{-21}$ cm/molecule for the 140.4 Pa spectrum and the root mean square deviation less than 5% in the whole range. This confirms the efficiency of the applied correction and allows for using either spectrum. To construct the global line list, we selected at least two spectra for each spectral interval, according to the absorption amplitude (see Fig. 2): the 13.2 Pa spectrum was used from 4850 to 5250 $cm^{-1}$, the 46 Pa spectrum in 4700-4850 $cm^{-1}$ and 5200-5300 $cm^{-1}$ regions, the 140.4 Pa in the 4700-5500 $cm^{-1}$ range, the 304 Pa spectrum from 5260 to 5600 $cm^{-1}$ and, the KP1 spectrum in the 5550-5650 $cm^{-1}$ range. The comparison between the 304 Pa and the KP1 spectra in the range 5550-5600 $cm^{-1}$ was used to calibrate in intensity the latter (Fig. 3).

Several water vapor lines (present as an impurity) were also observed in the spectra, accidentally hiding some ammonia lines above 5200 $cm^{-1}$. They were removed manually or subtracted from the spectrum by comparison with the $H_2O$ line list from the HITRAN2020 database [5]. Finally, the resulting ammonia list includes 9110 lines with intensity ranging between $1 \times 10^{-25}$ and $1.3 \times 10^{-20}$ cm/molecule including 505 $^{15}NH_3$ transitions (see lower panel of Fig. 1). In case of superposition of a $^{14}NH_3$ line and a $^{15}NH_3$ line (or a water line), the intensity of the interfering line was carefully estimated and subtracted in order to minimise its impact on the retrieval of the $^{14}NH_3$ line intensity.

As mentioned in Ref. [3], the FTS spectra under analysis do not correspond to the ammonia natural isotopic abundance but are enriched in the $^{15}NH_3$ isotopologue due to previous recordings with $^{15}N$ enriched gas samples. The $^{15}NH_3$ transitions in the different spectra were identified by comparison with a Kitt Peak spectrum highly enriched in $^{15}NH_3$ (Ref. 930826R0.016, $p$ = 2.00 Torr, $T$ = 23.8 °C, $L$ = 2.4 m with CO for calibration). The $^{15}NH_3$ relative abundance corresponding of our FTS spectra has been estimated in two ways: using the absolute intensities obtained in Ref. [13] already used in Ref. [3] or by comparison with the calculated intensity values of Ref. [14]. The two results agree and lead to the relative abundance values included in Table 1. The $^{15}NH_3$ abundance increases from 0.54% (340 Pa) to 0.78% (13.2 Pa) to be compared to a natural value of 0.366% [5]. As the four spectra were recorded successively by decreasing steps of the pressure, the isotopic ratio increased, due to the progressive desorption of $^{15}NH_3$ adsorbed on the walls of the cell and exchanges with ammonia in natural isotopic abundance initially injected in the cell. Note that the estimated value of the $^{15}NH_3$ abundance in the various analyzed spectra was used to scale the $^{15}NH_3$ line intensities accordingly, and the reported intensity values correspond to the natural abundance.

## 4. Rovibrational assignments

Following our recent analysis [1, 3, 4], the C2018 variational list of $^{14}NH_3$ [11] was used as a primary source for the rovibrational assignment of the experimental line list. The C2018 rovibrational labeling uses 13 quantum numbers:

$\nu_1, \nu_2, \nu_3, \nu_4, L_3, L_4, \tau_{inv}, \Gamma_{vib}, J, K, \Gamma_{rot}, N_B, \Gamma_{tot}$ where $\nu_i$ are the vibrational normal-mode quantum numbers, $L_i = |l_i|$ are the corresponding vibrational angular momentum quantum numbers, $\tau_{inv} = a/s$ is the inversion symmetry, and $\Gamma_{vib}$ is the symmetry of the vibrational motion. $J$ is the total angular-momentum quantum number, $K = |k|$ is the projection of the total angular momentum on the molecule-fixed axis $z$, and $\Gamma_{rot}$ is the rotational symmetry. Finally, $\Gamma_{tot}$ stands for the full symmetry of the eigenstate, and $N_B$ is the block counting number used during the generation of the C2018 list. Let us recall that only $J$ and $\Gamma_{tot}$ are exact quantum numbers, the others are approximate ones which describe helpfully the level considering its true wavefunction and how this wavefunction is projected on the basis set. In each $(J, \Gamma_{tot})$ subspace, the diagonalization process gives the eigenvalues and eigenstates which correspond to the energy levels, ordered by increasing energy and with a rank number $N_B$. In this context, let us mention the work of Huang *et al.* who have processed the same type of calculations, using a refined potential surface [15, 16]. The quality of the predicted energy positions is claimed to be improved compared to C2018 but the transition intensities are not provided.

The assignment process has been described in detail in our previous contributions [1, 3]. Coincidences between the experimental and C2018 lists were searched automatically with the constraints $\delta\nu = |\nu_{exp.} - \nu_{calc.}| \leq 1\,\mathrm{cm}^{-1}$ and $0.5 \leq S_{exp.}/S_{calc.} \leq 2$. For a given measured line, the C2018 candidates were tested using LSCD relations combined with intensity considerations. It means that the LSCD candidate partners were also subjected to the intensity screening with a similar criterion as for the initial C2018 match. For the search of LSCD relations, different studies extending from 3900 to 6500 $\mathrm{cm}^{-1}$ were considered [3, 4, 5]. The method of branches was used to complement the assignment procedure [3]. The (obs.-calc.) wavenumber differences within a given vibrational branch are expected to vary slowly with the rotational quantum numbers. This expected tendency was used to confirm the LSCD assignments and for transitions missing LSCD partners. In some cases, the application of the LSCD relations leads to an assignment of two or more C2018 predicted transitions to a single experimental line. In such a case, the original line was artificially split into the corresponding number of independent transitions with positions shifted by a negligible value of $1\times10^{-5}\,\mathrm{cm}^{-1}$. The intensities of these new transitions were obtained by affecting to each transition the fraction of the measured total intensity following the predictions of the C2018 line list.

Overall, 6562 out of 8610 transitions were assigned to 61 $^{14}NH_3$ vibrational bands listed in Table 2. In this table, the vibrational bands are defined by the vibrational quantum labels: $\nu_{1,2,3,4}$, $L_{1,2}$ and $\Gamma_{vib}$ (the $\tau_{inv}$ label has been added). The line assignments are included in the list provided as a Supplementary Material. Considering the C2018 intensities, the assigned transitions represent 98.9 % of the total integrated intensity in the region.

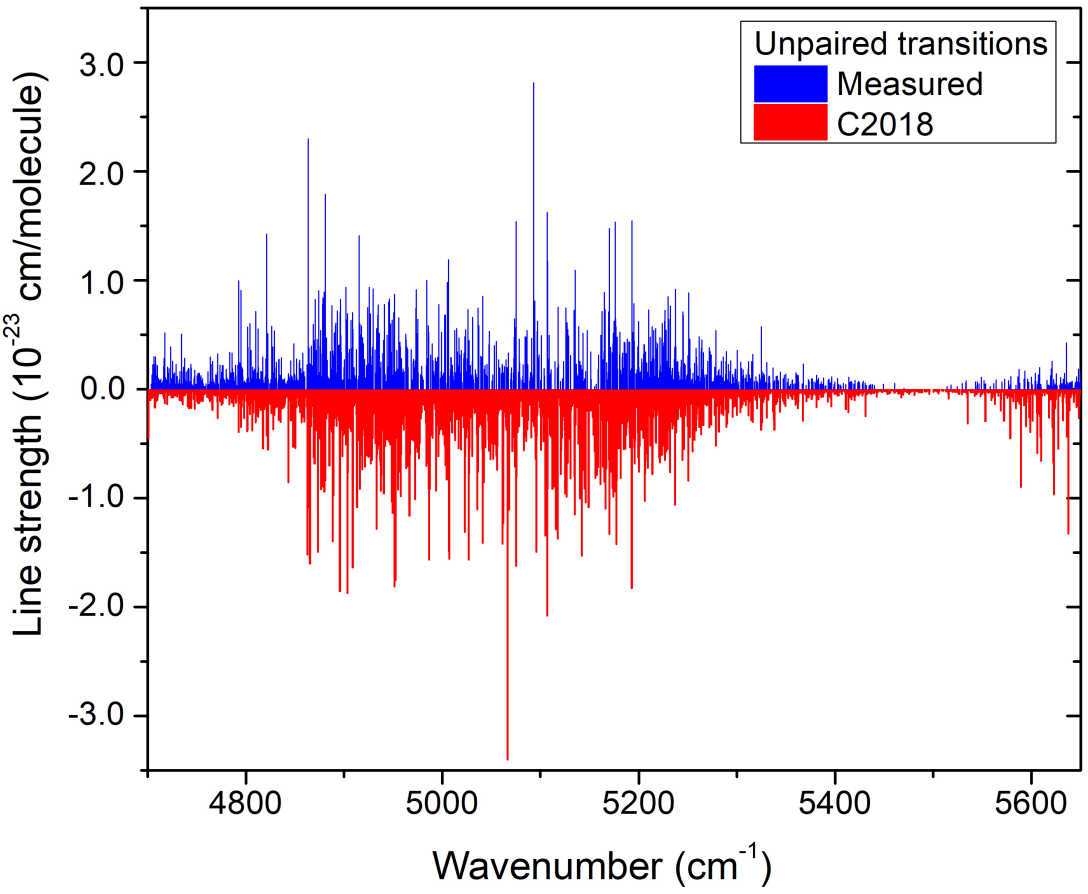


Figure 4: Comparison between the experimental lines left unassigned and the C2018 calculated lines of $^{14}NH_3$ with no experimental counterpart.

Table 2: Statistics and integrated absorption of the various vibrational bands contributing to the $^{14}NH_3$ spectrum between 4705 and 5650.3 $cm^{-1}$. The bands are ordered according to their C2018 integrated intensities.

| | C2018 | | | This work | | | | |
|---|---|---|---|---|---|---|---|---|
| Vibrational band[a] | $E_0$[b] ($cm^{-1}$) | $Nb$[c] | Band Int.[d] (cm/molecule) | $Nb$[e] | $J_{min}/J_{max}$[f] | Band Int.[g] (cm/molecule) | Int. ratio[h] (%) | $<\delta>$[i] ($cm^{-1}$) |
| $\nu_3^1+\nu_4^1$ (E′) s | 5052.6 | 1508 | 3.15E-19 | 911 | 0/17 | 3.16E-19 | 99.8 | 0.03 |
| $\nu_3^1+\nu_4^1$ (E″) a | 5053.2 | 1480 | 3.07E-19 | 909 | 0/17 | 3.08E-19 | 99.8 | 0.02 |
| $\nu_1+\nu_4^1$ (E′) s | 4955.8 | 1063 | 2.15E-20 | 564 | 0/14 | 2.18E-20 | 97.9 | 0.01 |
| $\nu_1+\nu_4^1$ (E″) a | 4956.9 | 1021 | 2.08E-20 | 525 | 0/15 | 2.11E-20 | 97.9 | 0.06 |
| $\nu_3^1+\nu_4^1$ ($A_1'$) s | 5067.8 | 552 | 1.56E-20 | 337 | 1/13 | 1.60E-20 | 98.8 | 0.04 |
| $\nu_3^1+\nu_4^1$ ($A_2''$) a | 5067.7 | 546 | 1.32E-20 | 324 | 0/13 | 1.33E-20 | 98.3 | 0.06 |
| $\nu_3^1+\nu_4^1$ ($A_2'$) s | 5052.0 | 577 | 6.62E-21 | 297 | 2/12 | 6.45E-21 | 96.2 | 0.01 |
| $\nu_3^1+\nu_4^1$ ($A_1''$) a | 5052.7 | 585 | 6.21E-21 | 299 | 2/13 | 6.12E-21 | 96.3 | 0.00 |
| $4\nu_2+\nu_4^1$ (E′) s | 5104.9 | 638 | 5.86E-21 | 161 | 4/11 | 5.42E-21 | 92.9 | 0.20 |
| $2\nu_2+2\nu_4^0$ ($A_2''$) a | 5093.6 | 402 | 5.03E-21 | 109 | 3/13 | 6.20E-21 | 96.0 | 0.17 |
| $\nu_2+\nu_3^1+\nu_4^1$ (E′) s ← $\nu_2$ | 5080.4 | 485 | 4.28E-21 | 257 | 0/14 | 4.20E-21 | 96.2 | -0.05 |
| $\nu_2+\nu_3^1+\nu_4^1$ (E″) a ← $\nu_2$ | 5104.1 | 467 | 3.25E-21 | 241 | 0/14 | 3.20E-21 | 95.6 | -0.10 |
| $2\nu_2+\nu_3^1$ (E′) s | 5144.9 | 706 | 2.89E-21 | 279 | 1/14 | 2.96E-21 | 86.3 | 0.21 |
| $\nu_1+2\nu_2$ ($A_1'$) s | 5000.2 | 448 | 2.47E-21 | 186 | 1/12 | 3.32E-21 | 92.0 | 0.19 |
| $2\nu_2+2\nu_4^2$ (E″) a | 5113.3 | 314 | 1.25E-21 | 58 | 4/15 | 1.06E-21 | 86.6 | 0.35 |
| $2\nu_2+\nu_3^1$ (E″) a | 5353.0 | 651 | 1.08E-21 | 368 | 0/12 | 9.92E-22 | 89.8 | 0.15 |
| $3\nu_4^1$ (E′) s | 4799.2 | 496 | 9.91E-22 | 42 | 4/16 | 4.02E-22 | 38.8 | 0.15 |
| $3\nu_4^1$ (E″) a | 4801.4 | 452 | 5.48E-22 | 13 | 3/16 | 7.24E-23 | 14.4 | -0.09 |
| $3\nu_4^3$ ($A_2'$) s | 4840.9 | 262 | 4.95E-22 | 52 | 2/10 | 3.46E-22 | 60.9 | 0.19 |
| $3\nu_4^3$ ($A_1'$) s | 4841.6 | 245 | 4.94E-22 | 46 | 1/13 | 4.16E-22 | 57.9 | 0.12 |
| $3\nu_4^3$ ($A_2''$) a | 4843.4 | 204 | 4.23E-22 | 30 | 0/12 | 4.08E-22 | 57.6 | 0.16 |
| $3\nu_4^3$ ($A_1''$) a | 4843.0 | 251 | 3.95E-22 | 27 | 6/11 | 1.51E-22 | 54.3 | 0.10 |
| $3\nu_2+\nu_3^1$ (E′) s ← $\nu_2$ | 4923.6 | 266 | 3.86E-22 | 121 | 1/11 | 3.11E-22 | 74.2 | 0.15 |
| $\nu_1+2\nu_2$ ($A_2''$) a | 5233.8 | 207 | 3.12E-22 | 58 | 0/12 | 1.94E-22 | 73.7 | 0.28 |
| $2\nu_2+2\nu_4^0$ ($A_1'$) s | 4756.9 | 163 | 1.80E-22 | 20 | 1/10 | 9.07E-23 | 48.0 | 0.16 |
| $2\nu_2+2\nu_4^2$ (E′) s | 4773.8 | 294 | 1.71E-22 | 4 | 5/9 | 6.60E-24 | 3.0 | 0.16 |
| $2\nu_2+\nu_3^1+\nu_4^1$ (E′) s ← $2\nu_2$ | 5119.8 | 179 | 1.67E-22 | 23 | 2/8 | 6.51E-23 | 38.7 | -0.20 |
| $\nu_2+\nu_3^1+\nu_4^1$ ($A_2''$) a ← $\nu_2$ | 5117.2 | 159 | 1.56E-22 | 31 | 2/10 | 1.04E-22 | 59.6 | -0.22 |
| $\nu_2+\nu_3^1+\nu_4^1$ ($A_1'$) s ← $\nu_2$ | 5091.8 | 159 | 1.50E-22 | 38 | 3/9 | 1.02E-22 | 63.8 | -0.29 |
| $\nu_2+\nu_3^1+\nu_4^1$ ($A_1''$) a ← $\nu_2$ | 5101.2 | 156 | 1.39E-22 | 33 | 2/9 | 7.75E-23 | 43.7 | -0.20 |
| $\nu_2+\nu_3^1+\nu_4^1$ ($A_2'$) s ← $\nu_2$ | 5075.6 | 113 | 1.20E-22 | 22 | 4/8 | 9.06E-23 | 63.6 | -0.22 |
| $\nu_1+\nu_2+\nu_4^1$ (E″) a ← $\nu_2$ | 4998.4 | 206 | 1.14E-22 | 25 | 1/9 | 4.55E-23 | 28.7 | -0.33 |
| $\nu_1+\nu_3^1$ (E′) s ← $\nu_4$ | 4982.5 | 267 | 1.09E-22 | 5 | 4/7 | 6.42E-24 | 5.8 | 0.02 |
| $\nu_1+\nu_2+\nu_4^1$ (E′) s ← $\nu_2$ | 4965.4 | 196 | 9.84E-23 | 15 | 2/10 | 2.37E-23 | 23.3 | -0.36 |
| $\nu_3^1+2\nu_4^2$ ($A_2''$) a ← $\nu_4$ | 5025.8 | 103 | 8.53E-23 | 1 | 6/6 | 1.58E-24 | 1.6 | 0.17 |
| $\nu_3^1+2\nu_4^2$ ($A_1''$) a ← $\nu_4$ | 5025.4 | 81 | 5.67E-23 | 1 | 4/4 | 1.96E-24 | 2.5 | 0.10 |
| $\nu_1+3\nu_2$ ($A_1'$) s ← $\nu_2$ | 4805.4 | 73 | 3.89E-23 | 33 | 1/8 | 2.98E-23 | 67.1 | 0.33 |
| $2\nu_2+\nu_3^1+\nu_4^1$ (E″) a ← $2\nu_2$ | 5355.5 | 105 | 3.44E-23 | 2 | 5/7 | 1.92E-24 | 3.6 | -0.10 |

*Continued on next page*

Table 2 – *Continued from previous page*

| Vibrational band[a] | C2018 $E_0$[b] ($cm^{-1}$) | C2018 $Nb$[c] | C2018 Band Int.[d] (cm/molecule) | This work $Nb$[e] | This work $J_{min}/J_{max}$[f] | This work Band Int.[g] (cm/molecule) | Int. ratio[h] (%) | $<\delta>$[i] ($cm^{-1}$) |
|---|---|---|---|---|---|---|---|---|
| $\nu_1 + 2\nu_4^0$ ($A_2''$) a $\leftarrow \nu_4$ | 4978.4 | 74 | 2.73E-23 | 1 | 3/3 | 1.15E-24 | 3.5 | 0.09 |
| $\nu_2 + \nu_3^1$ (E″) a | 4435.4 | 33 | 2.72E-23 | 13 | 11/14 | 2.05E-23 | 79.6 | 0.04 |
| $\nu_1 + 3\nu_2$ ($A_1'$) s | 5737.9 | 35 | 2.59E-23 | 21 | 4/8 | 2.79E-23 | 89.2 | 0.42 |
| $6\nu_2$ ($A_1'$) s $\leftarrow \nu_2$ | 5110.9 | 22 | 2.48E-23 | 4 | 8/9 | 1.87E-23 | 63.0 | 0.00 |
| $3\nu_2 + 2\nu_4^2$ (E′) s | 5622.6 | 61 | 2.30E-23 | 3 | 1/5 | 3.16E-24 | 11.9 | 0.87 |
| $4\nu_2 + \nu_4^1$ (E″) a | 5708.3 | 51 | 1.81E-23 | 1 | 7/7 | 2.52E-25 | 1.3 | 0.12 |
| $2\nu_2 + \nu_3^1 + \nu_4^1$ (E′) s $\leftarrow \nu_4$ | 5091.0 | 84 | 1.77E-23 | 1 | 6/6 | 6.06E-25 | 0.6 | -0.35 |
| $3\nu_2 + \nu_3^1$ (E″) a $\leftarrow \nu_2$ | 5398.9 | 79 | 1.72E-23 | 9 | 2/7 | 4.00E-24 | 21.6 | 0.11 |
| $\nu_2 + \nu_3^1$ (E′) s | 4416.9 | 25 | 1.54E-23 | 16 | 12/15 | 1.39E-23 | 90.9 | 0.12 |
| $3\nu_2 + \nu_3^1$ (E′) s | 5856.1 | 35 | 1.21E-23 | 5 | 7/9 | 5.37E-24 | 37.6 | 0.22 |
| $\nu_3^1 + 2\nu_4^2$ ($A_2''$) a $\leftarrow 2\nu_2$ | 5054.6 | 43 | 9.89E-24 | 1 | 6/6 | 8.00E-25 | 7.8 | 0.18 |
| $3\nu_2 + 2\nu_4^0$ ($A_2''$) a $\leftarrow \nu_2$ | 5201.1 | 17 | 9.56E-24 | 2 | 9/9 | 6.11E-24 | 40.2 | 0.27 |
| $\nu_1 + 3\nu_2$ ($A_2''$) a $\leftarrow \nu_2$ | 5297.9 | 35 | 6.86E-24 | 2 | 4/6 | 8.34E-25 | 8.7 | 0.57 |
| $\nu_1 + 2\nu_2 + \nu_4^1$ (E′) s $\leftarrow \nu_4$ | 4955.9 | 32 | 5.71E-24 | 1 | 6/6 | 5.03E-25 | 9.3 | -0.30 |
| $2\nu_2 + \nu_3^1 + \nu_4^1$ (E′) s $\leftarrow \nu_2$ | 5784.8 | 19 | 4.87E-24 | 1 | 6/6 | 4.80E-25 | 4.2 | -0.35 |
| $\nu_1 + \nu_2$ ($A_1'$) s | 4294.5 | 5 | 2.41E-24 | 3 | 12/13 | 2.10E-24 | 85.8 | 0.10 |
| $\nu_2 + 3\nu_4^3$ ($A_1'$) s | 5718.7 | 3 | 2.26E-24 | 1 | 4/4 | 1.35E-24 | 43.0 | 0.50 |
| $\nu_1 + \nu_2$ ($A_2''$) a | 4320.0 | 8 | 2.02E-24 | 4 | 12/14 | 1.40E-24 | 64.5 | 0.02 |
| $\nu_2 + 2\nu_4^2$ (E′) s | 4135.8 | 5 | 1.89E-24 | 1 | 13/13 | 8.83E-25 | 40.5 | 0.42 |
| $\nu_2 + 2\nu_4^2$ (E″) a | 4192.9 | 4 | 1.62E-24 | 2 | 11/13 | 1.10E-24 | 78.9 | 0.29 |
| $\nu_2 + 3\nu_4^3$ ($A_1'$) s $\leftarrow \nu_2$ | 4786.3 | 4 | 1.54E-24 | 1 | 4/4 | 5.74E-25 | 32.2 | 0.49 |
| $\nu_1 + 3\nu_2$ ($A_2''$) a $\leftarrow 2\nu_2$ | 4632.8 | 4 | 4.66E-25 | 1 | 6/6 | 1.15E-25 | 26.8 | 0.57 |
| $\nu_2 + 2\nu_4^0$ ($A_2''$) a | 4173.1 | 1 | 4.13E-25 | 1 | 12/12 | 2.88E-25 | 100.0 | -0.11 |
| Sum | | 16759 | 7.384E-19 | 6562 | | 7.389E-19 | . | |
| Others[j] | | 1182 | 0.005E-19 | 2048 | | 0.03E-19 | | |
| Total[k] | | 17941 | 7.389E-19 | 8610 | | 7.43E-19 | . | |

Notes:

[a] Vibrational band labeling: $\nu_i$ ($i = 1 - 4$) are the vibrational normal modes corresponding to the $\nu_1$ symmetric stretch, $\nu_2$ symmetric bend, $\nu_3$ the antisymmetric stretch and $\nu_4$ antisymmetric bend, respectively. $L_3 = |l_3|$ and $L_4 = |l_4|$ are the vibrational angular momentum quantum numbers of the $\nu_3$ and $\nu_4$ modes, respectively.

[b] Energy of the lowest level of the upper vibrational state (corresponding generally to $J = K = 0$ as calculated in the C2018 list. In the case of the hot bands, the $J = K = 0$ value of the lowest state was subtracted.

[c] Number of lines of the corresponding band with C2018 intensity larger than $1 \times 10^{-25}$ cm/molecule.

[d] Sum of the C2018 intensities of given band, larger than $1 \times 10^{-25}$ cm/molecule. Note that the C2018 intensities are calculated for pure $^{14}NH_3$.

[e] Number of lines of the corresponding band assigned in the studied spectrum.

[f] Minimum and maximum values of the rotational quantum numbers of the assigned lines.

[g] Sum of the experimental intensities derived from the optical depth, temperature and total pressure of the spectrum for the considered band.

[h] Ratio of the sum of the C2018 intensities of the transitions identified in the studied spectrum by the total C2018 intensity of the considered band.

[i] Average value of the (exp.- C2018) position differences of the considered band.

*Continued on next page*

Table 2 – *Continued from previous page*

| Vibrational band[a] | C2018 $E_0$[b] ($cm^{-1}$) | C2018 $Nb$[c] | C2018 Band Int.[d] (cm/molecule) | This work $Nb$[e] | This work $J_{min}/J_{max}$[f] | This work Band Int.[g] (cm/molecule) | Int. ratio[h] (%) | $<\delta>$[i] ($cm^{-1}$) |
|---|---|---|---|---|---|---|---|---|
| [j] For the C2018 line list, "others" correspond to the intensity sum of the predicted vibrational bands absent in the list, while for the experimental list of transitions, it corresponds to the intensity sum of unassigned transitions. Removing the $^{15}NH_3$ components, the measured intensities of the assigned transitions represent 99.5% of the total measured intensities. | | | | | | | | |
| [k] Note that the C2018 intensities of assigned transitions represent 98.85% of the total C2018 intensities in the region. | | | | | | | | |

Figure 4 compares the set of unassigned lines to that of the C2018 lines with no experimental counterpart. All unassigned lines have an intensity smaller than $2.5 \times 10^{-23}$ cm/molecule. Except for one transition, all the C2018 transitions with intensity above $2.5 \times 10^{-23}$ cm/molecule have been found. Overall, the appearance of the two data sets is similar. We nevertheless note that the unpaired C2018 transitions have a larger intensity than the unassigned lines at the high energy edge near 5600 $cm^{-1}$ while the situation is opposite near the low energy edge around 4800 $cm^{-1}$. Extra experimental absorption could be partly due to $NH_2D$ which has a natural abundance of about $3.4 \times 10^{-4}$ which leads to transitions with rough estimated intensity of a few $10^{-24}$ cm/molecule for the stronger lines. Let us recall that the identified $^{15}NH_3$ lines have been removed from the experimental panel.

## 5. Upper state energies of $^{14}NH_3$

By adding the lower state energies [9] to the measured experimental line positions, the upper state empirical energies of 2215 $^{14}NH_3$ rovibrational levels were derived from the assigned transitions. The determined upper levels were reached by up to 11 transitions. 560 levels were derived from a single transition, 496 from two transitions and the remaining (1151) from more than two transitions. In the last case, the average value and standard deviation were calculated in two ways, for all the transitions and for a 30% trimmed selection of them. In the last case, the *rms* of the standard deviation over the determined energies was reduced from $(0.9 \pm 1.8) \times 10^{-3}$ $cm^{-1}$ to $(0.3 \pm 0.3) \times 10^{-3}$ $cm^{-1}$. The list of derived energy levels is given in Supplementary Materials.

The determined $^{14}NH_3$ energy levels have been highlighted on Figure 5 which presents the overall set of C2018 energy values for upper states of transitions predicted in the 4705-5650 $cm^{-1}$ interval, with intensity larger than $1 \times 10^{-25}$ cm/molecule. The average rotational term $[9.7J(J+1) - 3.6K^2]$ have been subtracted for the clarity of the plot.

Three groups of energy levels are observed as upper levels of transitions located in our region of interest. Their reduced energies belong to the 4500-5500, 5500-6100 and 6100-7000 $cm^{-1}$ ranges depending if they were determined from cold transitions, hot transitions starting from $\nu_2$, hot transitions from $2\nu_2$ and $\nu_4$, respectively.

Among the 2215 upper state energy levels determined in this work, 1939 are new compared to the MARVEL set of levels of Ref. [9]. Figure 6 presents the differences between upper state energies and the calculated C2018 values, *versus* the quantity $[J + K/(J+1)]$. Except for a few outliers, the agreement with MARVEL values [9] is very good (average and *rms* values of $2 \times 10^{-4}$ and $7 \times 10^{-4}$ $cm^{-1}$ for the (MARVEL-exp.) differences, respectively). A small overestimation of the MARVEL values of $2 \times 10^{-4}$ $cm^{-1}$ is noted (right panel). As concerns the C2018 values [11], the deviations remain in a $\pm 0.6$ $cm^{-1}$ range.

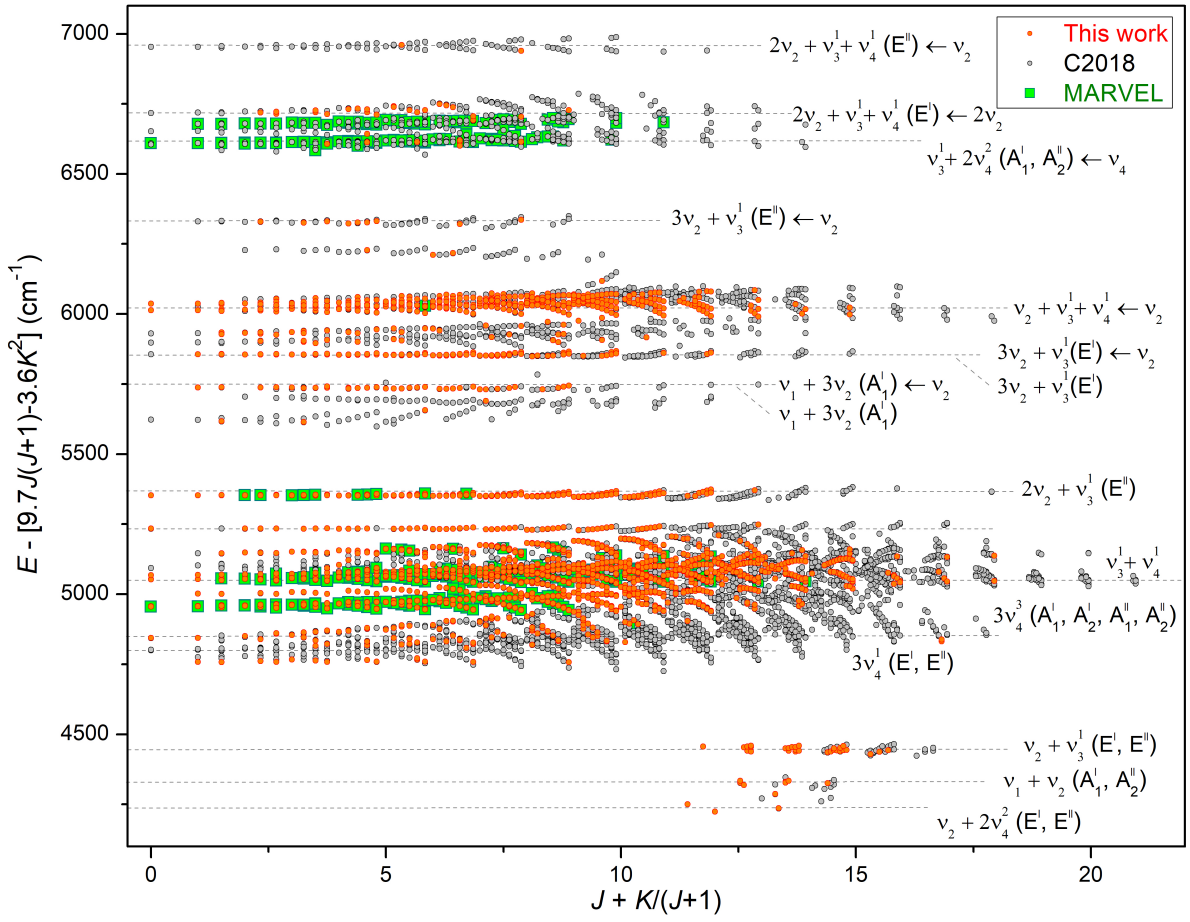


Figure 5: Upper state energies of the $^{14}NH_3$ transitions of the C2018 list in the 4705-5650 cm$^{-1}$ interval predicted with intensity larger than $1 \times 10^{-25}$ cm/molecule (grey dots). The average rotational term $[9.7J(J+1) - 3.6K^2]$ has been subtracted for clarity. The experimental values determined in this work are superimposed (orange dots) together with the existing empirical values provided by the MARVEL procedure (green squares)[9]. Some vibrational hot and cold bands from which the energies have been derived are indicated. Note that in some cases, the same upper levels are reached through both hot and cold bands.

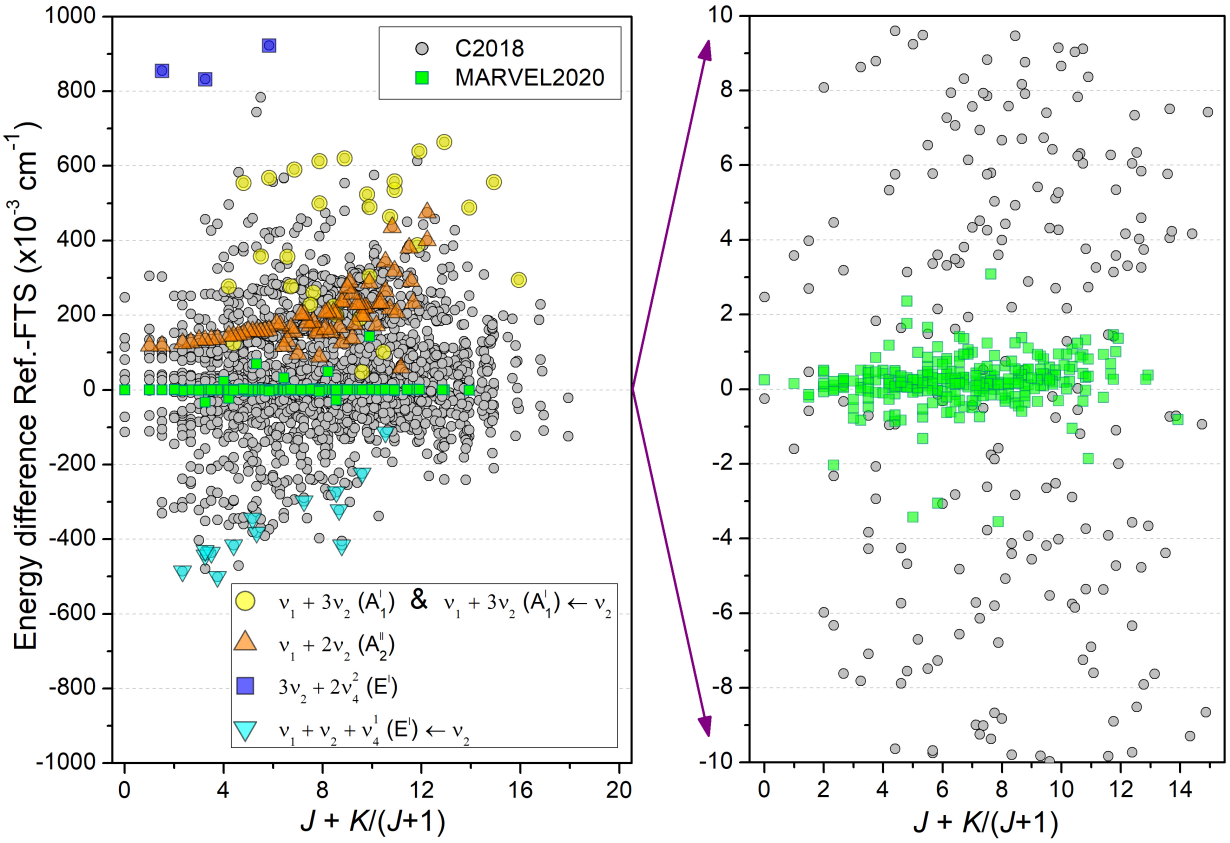


Figure 6: Differences between the C2018 [11] (grey) and MARVEL (green) [9] energies of the upper levels of $^{14}NH_3$ and the corresponding values derived in the present work. The values corresponding to upper levels derived from four vibrational bands are highlighted.

## 6. Comparison with the HITRAN line list

The overview comparison of our experimental list to the HITRAN2020 list (Fig. 1) illustrates the significant amount of new information provided by the analysis. Unassigned and assigned $^{14}NH_3$ lines, as well as minor $^{15}NH_3$ isotopologue lines can be distinguished on the plot. Our $^{14}NH_3$ line list includes about four times more lines than the HITRAN2020 list. As for the 3900-4700 $cm^{-1}$ range [3], the $^{15}NH_3$ transitions contribute to about 0.4% of the absorption in the studied range which is consistent with the natural relative abundance of 0.366% [5]. Note that both our work and HITRAN database do not consider the possible contribution of weak $NH_2D$ lines.

Table 3: Statistics and integrated absorption in various databases for ammonia in the 4703-5650.3 $cm^{-1}$ spectral range (intensity cut-off of $1 \times 10^{-25}$ cm/molecule at 296 K).

| | HITRAN2008[a] | | HITRAN2016 | | HITRAN2020 | | This work | | C2018 |
|---|---|---|---|---|---|---|---|---|---|
| | $^{14}NH_3$ | $^{15}NH_3$ | $^{14}NH_3$ | $^{15}NH_3$ | $^{14}NH_3$ | $^{15}NH_3$ | $^{14}NH_3$ | $^{15}NH_3$ | $^{14}NH_3$ |
| Transitions | 2001 | 129 | 1875 | 126 | 2493 | 126 | 8632 | 465 | 17941 |
| Assignments | 771 | 129 | 639 | 126 | 1255[b] | 126 | 6562 | 0 | 17941 |
| Intensity sum ($\times 10^{-19}$ cm/molecule) | 7.66 | 0.0146 | 7.65 | 0.0146 | 7.66 | 0.0146 | 7.42 | 0.034 | 7.39 |

Notes:

[a] 140 assignments were lost from the 2008 to 2016 editions of the HITRAN database with no explanation.

[b] This number is the sum of the HITRAN2016 transitions (639) and those added using the MARVEL process (616) [9].

In Fig. 7, a part of the 140.4 Pa spectrum is compared to a simulation based on the HITRAN2020 list around 5288 $cm^{-1}$. Transitions with experimental line parameters transferred from HITRAN2016 are distinguished from the transitions newly added through the MARVEL procedure. In general, the latters show a nice agreement in position and intensity. A number of additional lines are observed in our FTS spectrum illustrating the achieved sensitivity.

We have performed a systematic comparison of our assignments to those attached to the HITRAN2020 transitions. Among the 1275 transitions present in HITRAN2020 in our region, only 756 can be found within a 0.005 $cm^{-1}$ interval around the measured position value. Indeed, a significant number of HITRAN transitions missing in our list corresponds to newly added transitions with MARVEL line positions and C2018 intensities which are too weak to be detected in our spectra (see Fig. 1). 70 of the transitions with coincident positions show a large intensity disagreement. Part of these intensity mismatches might be due to accidental position coincidence between a weak HITRAN transitions with MARVEL origin and a strong measured line. Among the 686 remaining transitions in common, the assignment fully coincides for 362, is incompatible for 53 as $J'$ value differs and, for the remaining part (271), some differences are observed. For example, $J$ and $K$ are correct but the vibrational assignment is different, mainly interchanged between $\nu_1 + \nu_4$ and $\nu_3 + \nu_4$ above $J = 7$.

## 7. Intensity considerations

As the assignment process is supported by the intensity matching between the experimental spectrum and the C2018 calculations, it is important to discuss their level of agreement. The corresponding intensity ratios are plotted in Fig. 8 where the values relative to the main vibrational bands - $\nu_3 + \nu_4$ (E), $\nu_1 + \nu_4$ (E) and $\nu_3 + \nu_4$ (A)) - are highlighted. These bands represent 63.5 % of the total number of assigned transitions but bring 95.4 % of the total intensity. Overall, the agreement between the experimental

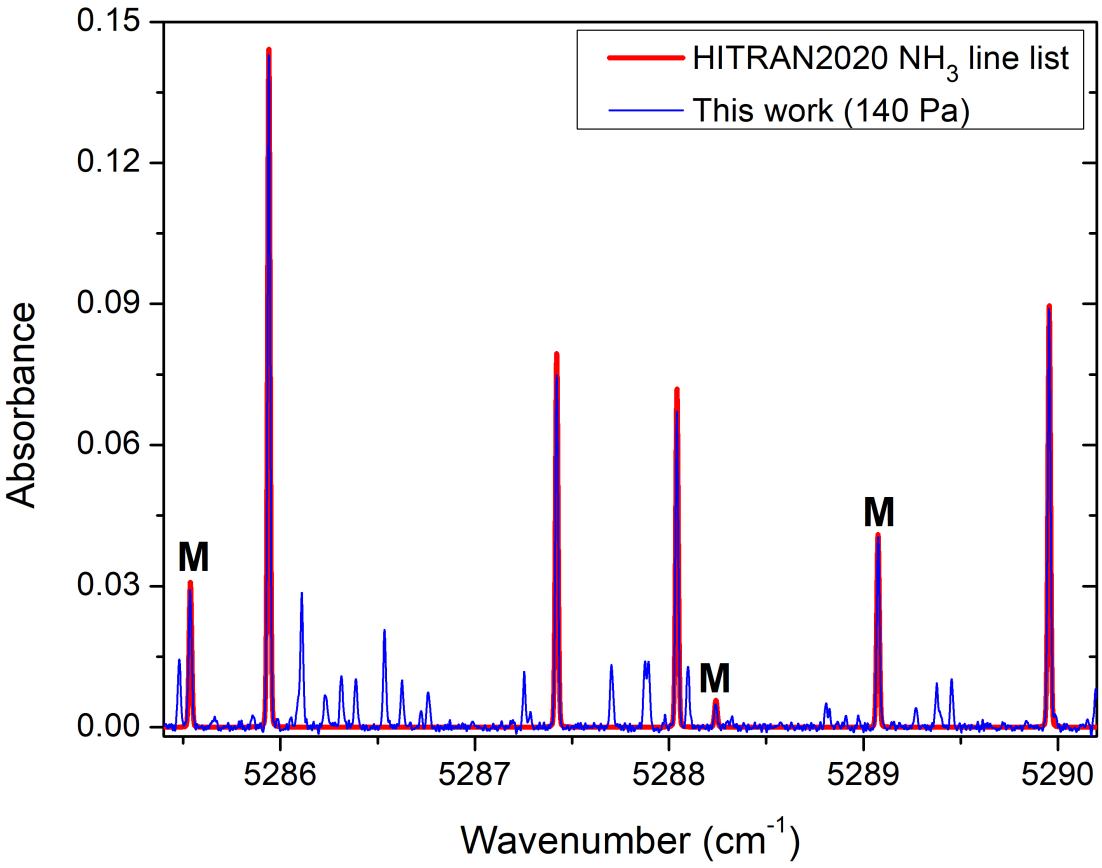


Figure 7: FTS spectrum at 140.4 Pa in the 5285-5290 $cm^{-1}$ range (blue line) compared to HITRAN2020 simulation (red): four lines came from experimentally observed data and were present in HITRAN2016 issue, and three lines indicated with a "M" corresponds to transitions added in HITRAN2020 from MARVEL process [8]. All the other lines are not present in HITRAN2020.

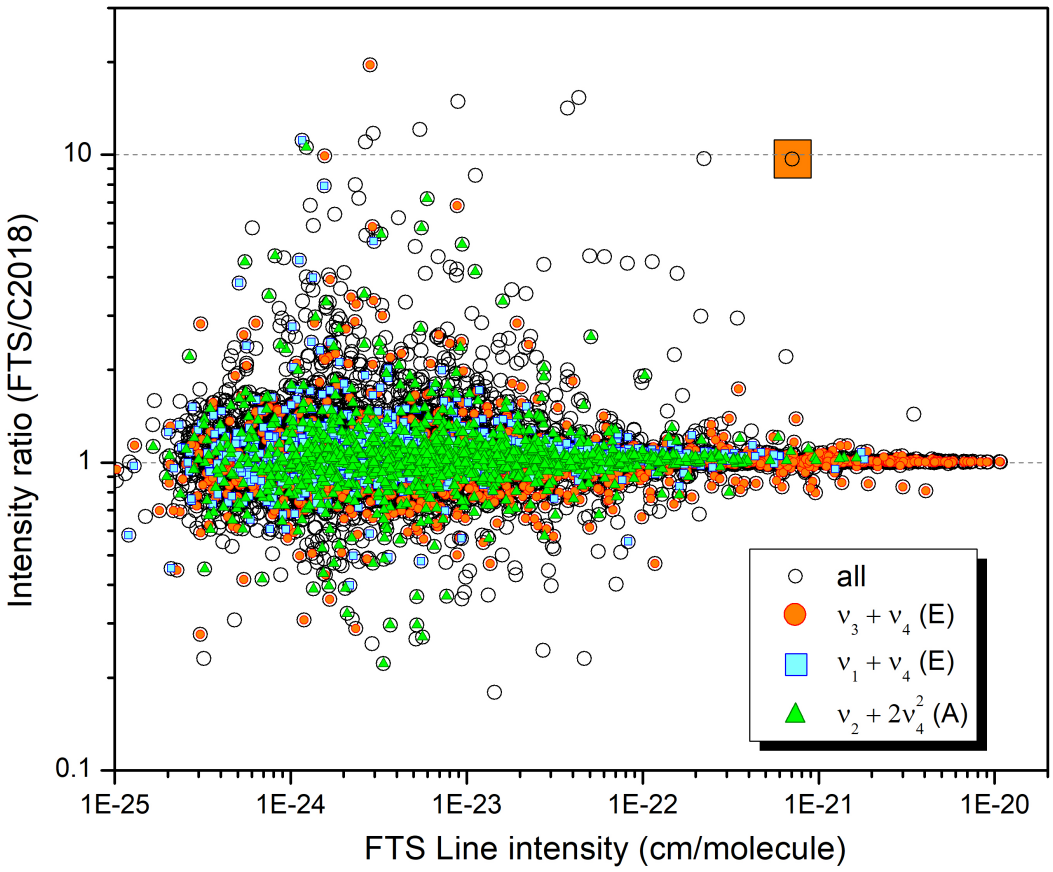


Figure 8: Ratios of the $^{14}NH_3$ line intensities measured in this work in the 4705-5650 $cm^{-1}$ spectral region to the corresponding C2018 values [11]. The intensity ratios corresponding to the $\nu_3 + \nu_4$ (E), $\nu_1 + \nu_4$ (E) and $\nu_3 + \nu_4$ (A) strong bands are distinguished (red, blue and green, respectively). The highlighted outlier corresponding to a strongly underestimated C2018 intensity is discussed in the text as an example of intensity transfer.

and calculated values is excellent. The increase of the dispersion for small line intensities is a usual phenomenon partly due to the larger relative uncertainty of the small experimental intensity values. However, there are some cases of strong transitions showing a large disagreement as for example, the transition measured at 4967.3479 $cm^{-1}$ with intensity of $7.09 \times 10^{-22}$ cm/molecule, (orange square on Fig. 8) which is predicted to have a ten times smaller C2018 intensity. This particular example is analyzed in details just below.

Remember that the first step of the assignment process is to associate C2018 and experimental lines with similar intensities and close line centers. Obviously, in the considered example, the intensity mismatch prevented the association to the C2018 transition with closest position. Nevertheless, loosening the intensity criterion, the LSCD search gives a reasonable agreement for the C2018 transition at 4967.2327 $cm^{-1}$ with a smaller intensity of $7.3 \times 10^{-23}$ cm/molecule. This transition belonging to the $\nu_1 + 2\nu_2$ vibrational band starts from $J = 7$, $K = 6$ $s$ level and reaches $J = 6$, $K = 3$ $s$ upper level with an energy of 5389.6889 $cm^{-1}$. The systematic search for the LSCD partners revealed three hot band transitions assigned in our previous study at lower energy [3] and four matches in the interval presently studied, thus confirming the assignment in spite of a strong underestimation of the

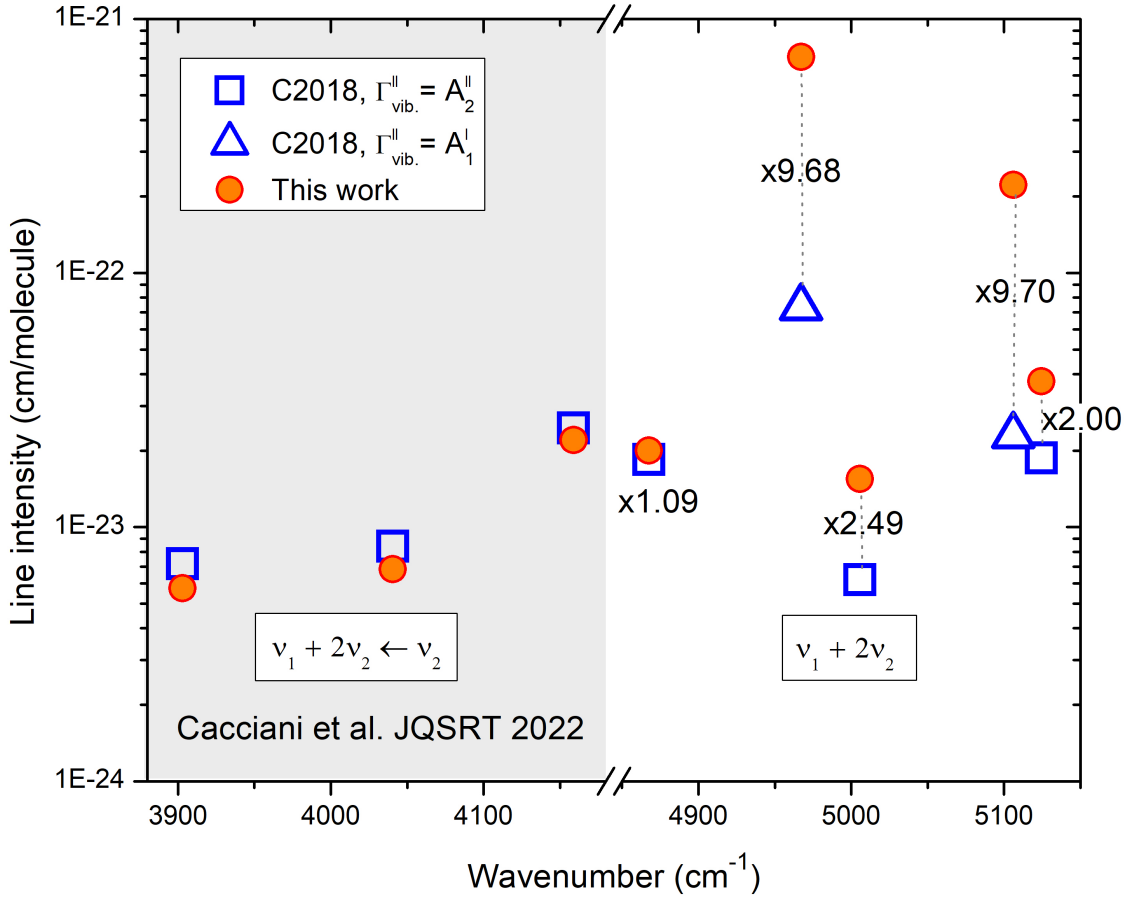


Figure 9: Calculated [11] and experimental transitions reaching the $N_B = 80$ upper level of the block ($J = 6$, $\Gamma_{tot} = A_2''$ at 5389.6889 cm$^{-1}$). The experimental transitions of the $\nu_1 + 2\nu_2 - \nu_2$ band were reported in Ref. [1] while the $\nu_1 + 2\nu_2$ cold band transitions are observed in the present work. The transition under study is the one at 4967.3479 cm$^{-1}$ with a C2018 intensity underestimated by a factor of 9.68. The C2018 values are plotted with different symbols (open squares and open triangles) according to the inversion symmetry ($a$ or $s$, respectively) of the lower state. The corresponding exp./C2018 intensity ratios are indicated for each transition. The experimental counterparts (orange circles) were found in this work and in Ref. [3].

C2018 intensity. While the hot transitions show an almost perfect intensity agreement, the FTS/C2018 intensity ratio for the five $\nu_1 + 2\nu_2$ band transitions vary from 1.09 up to 9.7 (Fig.9).

Let us recall that the only two good quantum numbers for $^{14}NH_3$ are $J$ and $\Gamma_{tot}$. The other labels given in C2018 list are only approximate. In fact, each wavefunction is found through the diagonalization of the Hamiltonian inside $J$, $\Gamma_{tot}$ blocks and is expressed as a linear combination of basis wavefunctions characterized by ($J$, $\Gamma_{tot}$) and completed by quantum labels $\nu_1$, $\nu_2$, $\nu_3$, $\nu_4$, $L_3$, $L_4$, $\tau_{inv}$, $K$, $\Gamma_{vib}$, $\Gamma_{rot}$. The labeling is completed by the rank in the block, $N_B$, which unambiguously designates the $N_B^{th}$ level of the ($J$, $\Gamma_{tot}$) block ordered by increasing value of the energy. The upper state involved in the discussed example corresponds to $N_B = 80$ in the (6, $A_2'$) block and has an experimental energy of 5389.80603 cm$^{-1}$. The experimental value of the energy separation from the next $N_B = 81$ level is only 0.225 cm$^{-1}$. The $N_B = 81$ upper state is the upper state of strong transitions and we interpret the large intensity of the $\nu_1 + 2\nu_2$ transitions reaching the $N_B = 80$ level as due to an intensity borrowing from those involving the $N_B = 81$ levels. It is interesting to note that the energy separation of the $N_B = 80$ and $N_B = 81$ levels is significantly smaller than its

C2018 value of 0.2945 $cm^{-1}$. This closer energetic resonance might explain the fact that the resulting intensity transfer is much larger than predicted by theory.

Table 4 presents the experimental and calculated energies and intensities of the five LSCD pairs of the $\nu_1 + 2\nu_2$ band together with the corresponding intensity ratios. If we sum the experimental intensities of the doublets of transitions reaching the $N_B = 80$ and 81 levels (last set of columns in Tab. 4), and compare them to the corresponding C2018 sums, an agreement within the experimental error bar (5%) is obtained.

Table 4: An example of C018 intensity transfer between the transitions arriving into two close upper states of the same $J'$, $\Gamma'_{tot}$ subspace.

| Lower State | | | | Upper state | | | | | | | | Sums and ratio | | |
|---|---|---|---|---|---|---|---|---|---|---|---|---|---|---|
| | | | | $J' = 6, \Gamma'_{tot} = A''_2, N'_B = 80$<br>$E'_{C2018} = 5389.6889\,cm^{-1}$<br>$E'_{emp} = 5389.80603\,cm^{-1}$ | | | | $J' = 6, \Gamma'_{tot} = A''_2, N'_B = 81$<br>$E'_{C2018} = 5389.9834\,cm^{-1}$<br>$E'_{emp} = 5390.03104\,cm^{-1}$ | | | | | | |
| $J''$ | $\tau''_{inv}$ | $N''_B$ | $E''_{C2018}$ ($cm^{-1}$) | $\nu_{TW}$ ($cm^{-1}$) | $S_{TW}$ (cm/mol.) | $S_{2018}$ (cm/mol.) | $r_{TW/C2018}$ | $\nu_{TW}$ ($cm^{-1}$) | $S_{TW}$ (cm/mol.) | $S_{C2018}$ (cm/mol.) | $r_{TW/C2018}$ | $\Sigma_{C2018}$ (cm/mol.) | $\Sigma_{TW}$ (cm/mol.) | $r_\Sigma$ |
| 7 | a | 2 | 522.2222 | 4867.5832 | 2.00E-23 | 1.85E-23 | 1.09 | | | 1.07E-24 | | 1.95E-23 | 2.00E-23 | 1.03 |
| 7 | s | 1 | 422.4562 | 4967.3479 | 7.09E-22 | 7.32E-23 | 9.68 | 4967.5729 | 3.01E-21 | 3.62E-21 | 0.83 | 3.69E-21 | 3.72E-21 | 1.01 |
| 6 | a | 2 | 383.9772 | 5005.8282 | 1.55E-23 | 6.21E-24 | 2.49 | 5006.0535 | 1.25E-23 | 2.27E-23 | 0.55 | 2.89E-23 | 2.80E-23 | 0.97 |
| 6 | s | 1 | 283.5719 | 5106.2317 | 2.22E-22 | 2.29E-23 | 9.70 | 5106.4570 | 9.59E-22 | 1.20E-21 | 0.80 | 1.23E-21 | 1.18E-21 | 0.96 |
| 5 | a | 1 | 265.2263 | 5124.5797 | 3.75E-23 | 1.87E-23 | 2.00 | 5124.8042 | 3.12E-23 | 5.42E-23 | 0.58 | 7.29E-23 | 6.86E-23 | 0.94 |

The situation observed for the $N_B = 80$ and 81 pair of levels is not isolated and many other cases of intensity transfer were found during the assignment process. This is also the case in other spectral regions. For instance, some examples can be found in our preceding study in the 5650-6300 $cm^{-1}$ range [1] and, Huang *et al.* [17] pointed out two similar occurrences in their re-analysis of the ammonia spectrum in this region.

Let us now try to select systematically the states with possible interaction with their nearby states in our range of interest. In the 4705-5650 $cm^{-1}$ interval, 1061 doublets of transitions with intensity above $1 \times 10^{-25}$ cm/molecule have been found in the C2018 list with upper energy levels separated by less than 2 $cm^{-1}$ (in identical blocks). In addition, 115 triplets, 16 quadruplets and 2 quintuplets fulfill this criterion. Loosening the transition cut-off, the number of possibly interacting transitions groups rises up to 1724 from previously mentioned 1194 ones. Comparing this list to our dataset we have found all experimental counterparts for 266 cases (250 doublets, 13 triplets and 3 quadruplets).

To test possible intensity transfer within the identified multiplets, we present in the upper panel of Fig. 10 the exp./C2018 intensity ratios with different symbols for the transitions reaching the resonant multiplets and the isolated levels. The first observation is that most of the large deviations correspond to resonant levels. In the lower panel of Fig. 10, we plotted the ratios for the intensity sum of the resonant transitions. The obtained result is impressive: while a significant fraction of the individual components show important disagreement between the experimental and C2018 intensities, their intensity sums coincide very well. We believe that the sensitivity of the wavefunctions to small inaccuracies of the potential energy surface could explain the phenomenon: a small variation of the energy separation of the interacting upper levels leads to a large intensity change for the weak component of the resonant doublets but the resulting intensity transfer does not affect the intensity sum of the involved transitions. Note that at higher energy the number of resonances within blocks increases sharply leading to more frequent intensity transfers and might degrade the agreement with C2018 intensity calculations. The results presently obtained can be used to improve future theoretical predictions of line intensities at higher energy.

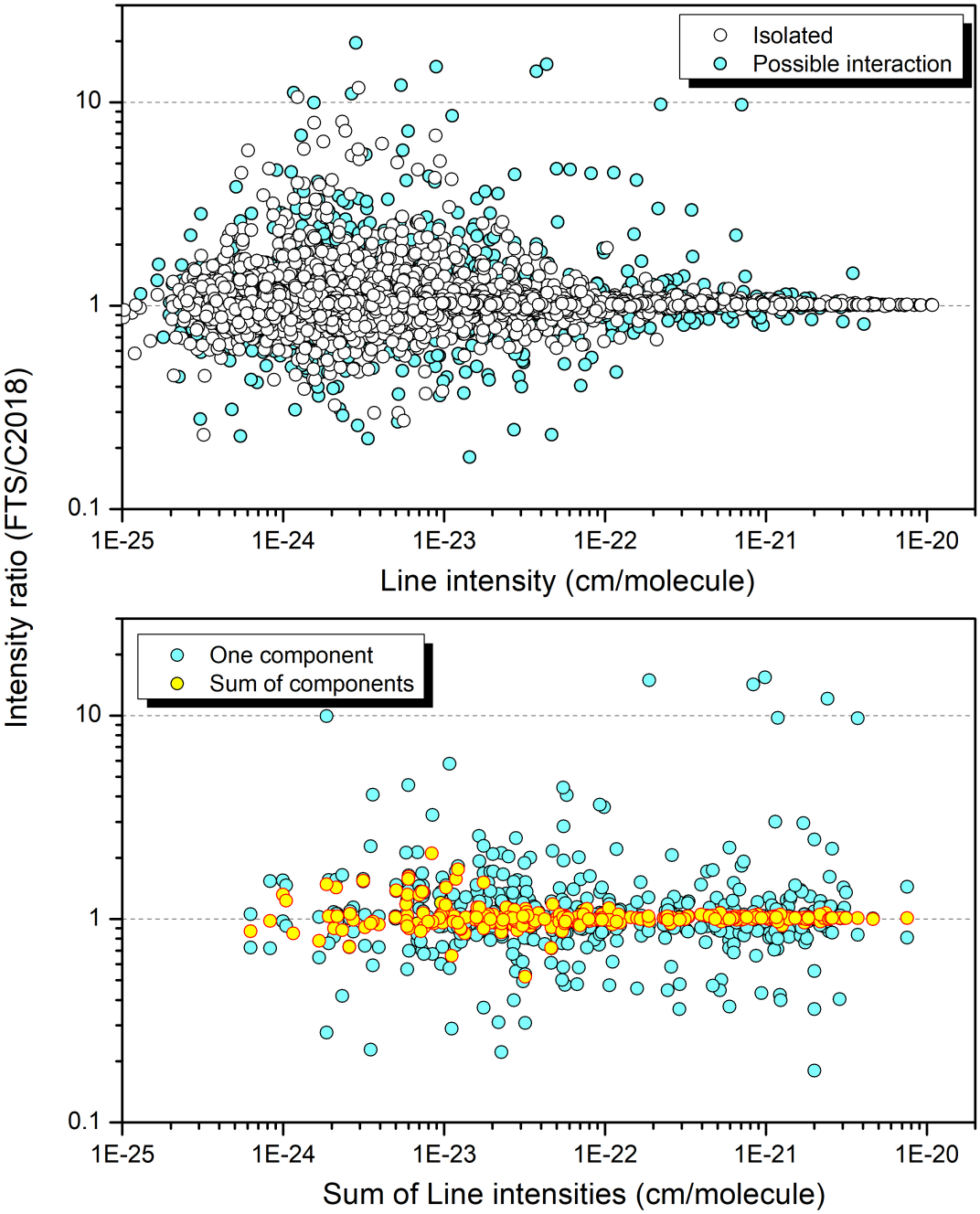


Figure 10: Upper panel: $S_{exp.}/S_{C2018}$ intensity ratios for the $^{14}NH_3$ transitions assigned in the 4705-5650 $cm^{-1}$ region. According to the energy separation of the upper energy level in a given ($J'$, $\Gamma'_{tot}$) subspace, a different symbol is used: black circles and cyan points when the energy separation from the neighbour level is more or less than 2 $cm^{-1}$, respectively. Lower panel: Intensity ratios for cases when all the possibly interacting components in a given group (belonging to the same $J'$, $\Gamma'_{tot}$ with $\Delta E < 2\,cm^{-1}$ and sharing the same lower state) were identified experimentally, individual ratio (cyan dots) and ratio of corresponding intensity sums (red /yellow dots).

## 8. Conclusion

New high resolution and low-pressure FTS recordings have allowed an in depth analysis of the room temperature ammonia spectrum from 4703 to 5650.3 $cm^{-1}$ range. Among the 9110 measured lines, 505 are identified as due to $^{15}NH_3$ minor isotopologue, and a rovibrational assignment is proposed for 6562 $^{14}NH_3$ lines. This is a significant improvement compared to the HITRAN2020 list [5], which provides 2493 $^{14}NH_3$ transitions (with 1255 assignments), 626 of them predicted by theory and not experimentally observed. Overall, our assigned transitions belong to 35 cold and 26 hot bands and bring over 98.8% of the integrated absorption in the region. 2215 upper energies were derived with accuracy better than 0.001 $cm^{-1}$. Among them 1939 are new, compared to those derived in Ref. [9] using the MARVEL procedure. A recommended list of 9110 transitions for ammonia in natural isotopic abundance is provided as Supplementary Material. The $^{14}NH_3$ line positions were calculated using our best empirical determination of the upper energy levels (estimated accuracy on the order of $5 \times 10^{-4}$ $cm^{-1}$). Despite the quality of *ab initio* calculations to accurately predict position and intensity of the $^{14}NH_3$ transitions [11] and the power of the Lower State Combination Difference technique to assign them, a number of important disagreements between the measured and C2018 intensities was evidenced. Most of the intensity mismatches concern weak transitions reaching an upper level with a close lying neighbour level reached by a stronger transition. As the intensity sum of the two interacting transitions coincides with the C2018 predictions, we conclude that the problematic situations result from intensity transfer between interacting multiplets. In those situations, line intensities provide a sensitive tool to reveal small inaccuracies of the potential energy surface used to generate the C2018 list [11]. As a result, the intensity agreement with C2018 calculations which is in general highly valuable for rovibrational assignment, should be used with caution, in particular at higher energy where the level density increases rapidly making resonance interactions more and more probable. In particular, the rovibrational assignments of the ammonia spectrum in the 1.5 $\mu$m range (6300-7000 $cm^{-1}$) already studied in Refs. [18, 19] might be extended by a careful consideration of possible intensity transfers.

## Declaration of competing interest

The authors declare that they have no known competing financial interests or personal relationships that could have appeared to influence the work reported in this paper.

## CRediT authorship contribution statement

**P. Cacciani:** Investigation. **P. Čermák:** Investigation. **J. Vander Auwera:** Investigation. **A. Campargue:** Investigation.

## Acknowledgments

This research was supported by the joint Slovak-Czech-French Danube Region project (DS-FR-19–0050), and by the Slovak Research and Development Agency (contract number APVV-19-0386). This work was also a contribution of the CPER research project CLIMIBIO. The authors thank the French Ministère de l'Enseignement Supérieur et de la Recherche, the Hauts de France Region and the European Funds for Regional Economic Development for their financial support to this project. This work was performed in the frame of the ANR project e_PYTHEAS (ANR-16-CE31-00 5).

# References


[1] P. Čermák, P. Cacciani, J. Cosléou, Accurate $^{14}NH_3$ line-list for the 2.3 $\mu$m spectral region, Journal of Quantitative Spectroscopy and Radiative Transfer 274 (2021) 107861. doi:10.1016/j.jqsrt.2021.107861.

[2] S. Serjeant, M. Elvis, G. Tinetti, The future of astronomy with small satellites, Nature Astronomy 4 (2020) 1031–1038. doi:10.1038/s41550-020-1201-5.

[3] P. Cacciani, Čermák P., J. Vander Auwera, A. Campargue, The ammonia absorption spectrum between 3900 and 4700 $cm^{-1}$, Journal of Quantitative Spectroscopy and Radiative Transfer 277 (2022) 107961. doi:10.1016/j.jqsrt.2021.107961.

[4] P. Cacciani, P. Čermák, S. Béguier, A. Campargue, The absorption spectrum of ammonia between 5650 and 6350 $cm^{-1}$, Journal of Quantitative Spectroscopy and Radiative Transfer 258 (2021) 107334. doi:10.1016/j.jqsrt.2020.107334.

[5] I. Gordon, L. Rothman, R. Hargreaves, R. Hashemi, E. Karlovets, F. Skinner, E. Conway, C. Hill, R. Kochanov, Y. Tan, P. Wcisło, A. Finenko, K. Nelson, P. Bernath, M. Birk, V. Boudon, A. Campargue, K. Chance, A. Coustenis, B. Drouin, J. Flaud, R. Gamache, J. Hodges, D. Jacquemart, E. Mlawer, A. Nikitin, V. Perevalov, M. Rotger, J. Tennyson, G. Toon, H. Tran, V. Tyuterev, E. Adkins, A. Baker, A. Barbe, E. Canè, A. Császár, A. Dudaryonok, O. Egorov, A. Fleisher, H. Fleurbaey, A. Foltynowicz, T. Furtenbacher, J. Harrison, J. Hartmann, V. Horneman, X. Huang, T. Karman, J. Karns, S. Kassi, I. Kleiner, V. Kofman, F. Kwabia–Tchana, N. Lavrentieva, T. Lee, D. Long, A. Lukashevskaya, O. Lyulin, V. Makhnev, W. Matt, S. Massie, M. Melosso, S. Mikhailenko, D. Mondelain, H. Müller, O. Naumenko, A. Perrin, O. Polyansky, E. Raddaoui, P. Raston, Z. Reed, M. Rey, C. Richard, R. Tóbiás, I. Sadiek, D. Schwenke, E. Starikova, K. Sung, F. Tamassia, S. Tashkun, J. Vander Auwera, I. Vasilenko, A. Vigasin, G. Villanueva, B. Vispoel, G. Wagner, A. Yachmenev, S. Yurchenko, The HITRAN2020 molecular spectroscopic database, Journal of Quantitative Spectroscopy and Radiative Transfer 277 (2022) 107949. doi:10.1016/j.jqsrt.2021.107949.

[6] L. Brown, J. Margolis, Empirical line parameters of $NH_3$ from 4791 to 5294 $cm^{-1}$, Journal of Quantitative Spectroscopy and Radiative Transfer 56 (2) (1996) 283–294. doi:10.1016/0022-4073(96)00041-6.

[7] I. Gordon, L. Rothman, C. Hill, R. Kochanov, Y. Tan, P. Bernath, M. Birk, V. Boudon, A. Campargue, K. Chance, B. Drouin, J.-M. Flaud, R. Gamache, J. Hodges, D. Jacquemart, V. Perevalov, A. Perrin, K. Shine, M.-A. Smith, J. Tennyson, G. Toon, H. Tran, V. Tyuterev, A. Barbe, A. Császár, V. Devi, T. Furtenbacher, J. Harrison, J.-M. Hartmann, A. Jolly, T. Johnson, T. Karman, I. Kleiner, A. Kyuberis, J. Loos, O. Lyulin, S. Massie, S. Mikhailenko, N. Moazzen-Ahmadi, H. Müller, O. Naumenko, A. Nikitin, O. Polyansky, M. Rey, M. Rotger, S. Sharpe, K. Sung, E. Starikova, S. Tashkun, J. V. Auwera, G. Wagner, J. Wilzewski, P. Wcisło, S. Yu, E. Zak, The HITRAN2016 molecular spectroscopic database, Journal of Quantitative Spectroscopy and Radiative Transfer 203 (2017) 3–69. doi:10.1016/j.jqsrt.2017.06.038.

[8] P. A. Coles, S. N. Yurchenko, J. Tennyson, ExoMol molecular line lists - XXXV. A rotation-vibration line list for hot ammonia, Monthly Notices of the Royal Astronomical Society 490 (4) (2019) 4638–4647. doi:10.1093/mnras/stz2778.

[9] T. Furtenbacher, P. A. Coles, J. Tennyson, S. N. Yurchenko, S. Yu, B. Drouin, R. Tóbiás, A. G. Császár, Empirical rovibrational energy levels of ammonia up to 7500 $cm^{-1}$, Journal of Quantitative Spectroscopy and Radiative Transfer 251 (2020) 107027. doi:10.1016/j.jqsrt.2020.107027.

[10] M. J. Down, C. Hill, S. N. Yurchenko, J. Tennyson, L. R. Brown, I. Kleiner, Re-analysis of ammonia spectra: Updating the HITRAN $^{14}NH_3$ database, Journal of Quantitative Spectroscopy and Radiative Transfer 130 (2013) 260–272. doi:10.1016/j.jqsrt.2013.05.027.

[11] P. A. Coles, R. I. Ovsyannikov, O. L. Polyansky, S. N. Yurchenko, J. Tennyson, Improved potential energy surface and spectral assignments for ammonia in the near-infrared region, Journal of Quantitative Spectroscopy and Radiative Transfer 219 (2018) 199–212. doi:10.1016/j.jqsrt.2018.07.022.

[12] C. A. Beale, A. Wong, P. Bernath, Infrared transmission spectra of hot ammonia in the 4800–9000 $cm^{-1}$ region, Journal of Quantitative Spectroscopy and Radiative Transfer 246 (2020) 106911. doi:10.1016/j.jqsrt.2020.106911.

[13] P. Čermák, J. Hovorka, P. Veis, P. Cacciani, J. Cosléou, J. El Romh, M. Khelkhal, Spectroscopy of $^{14}NH_3$ and $^{15}NH_3$ in the 2.3$\mu$m spectral range with a new VECSEL laser source, Journal of Quantitative Spectroscopy and Radiative Transfer 137 (2014) 13–22. doi:10.1016/j.jqsrt.2014.01.005.

[14] S. N. Yurchenko, A theoretical room-temperature line list for $^{15}NH_3$, Journal of Quantitative Spectroscopy and Radiative Transfer 152 (2015) 28–36. doi:10.1016/j.jqsrt.2014.10.023.

[15] X. Huang, D. W. Schwenke, T. J. Lee, Rovibrational spectra of ammonia. I. Unprecedented accuracy of a potential energy surface used with nonadiabatic corrections, The Journal of Chemical Physics 134 (4) (2011) 044320. doi:10.1063/1.3541351.

[16] X. Huang, D. W. Schwenke, T. J. Lee, Rovibrational spectra of ammonia. II. Detailed analysis, comparison, and prediction of spectroscopic assignments for $^{14}NH_3$, $^{15}NH_3$ , and $^{14}ND_3$, The Journal of Chemical Physics 134 (4) (2011) 044321. doi:10.1063/1.3541352.

[17] X. Huang, S. K., G. C. Toon, D. W. Schwenke, T. J. Lee, A collaborative $^{14}NH_3$ IR spectroscopic analysis at 6000 $cm^{-1}$, Journal of Quantitative Spectroscopy and Radiative Transfer 280 (2022) 108076. doi:10.1016/j.jqsrt.2022.108076.

[18] P. Cacciani, P. Čermák, J. Cosléou, J. El Romh, J. Hovorka, M. Khelkhal, Spectroscopy of ammonia in the range 6626–6805 $cm^{-1}$: using temperature dependence towards a complete list of lower state energy transitions, Molecular Physics 112 (18) (2014) 2476–2485. doi:10.1080/00268976.2014.924653.

[19] K. Sung, L. R. Brown, X. Huang, D. W. Schwenke, T. J. Lee, S. L. Coy, K. K. Lehmann, Extended line positions, intensities, empirical lower state energies and quantum assignments of $NH_3$ from 6300 to 7000 $cm^{-1}$, Journal of Quantitative Spectroscopy and Radiative Transfer 113 (11) (2012) 1066–1083, three Leaders in Spectroscopy. doi:10.1016/j.jqsrt.2012.02.037.